PHYSICAL REVIEW B **73**, 094406 (2006)

Magnetic phase diagram and demagnetization processes in perpendicular exchange-spring multilayers

G. Asti, M. Ghidini, R. Pellicelli, C. Pernechele, and M. Solzi
Dipartimento di Fisica, Università di Parma, Parco Area delle Scienze 7/A, 43100 Parma, Italy and CNISM, Parma, Italy

F. Albertini, F. Casoli, S. Fabbrici, and L. Pareti
Istituto IMEM-CNR, Parco Area delle Scienze 37/A, 43010 Fontanini, Parma, Italy

(Received 13 September 2005; revised manuscript received 17 January 2006; published 8 March 2006)

The magnetic behavior of the perpendicular exchange-spring bilayer and multilayer, constituted of a hard and a soft phase that are exchange-coupled on a nanometric scale, is analyzed by a one-dimensional micromagnetic model leading to a complete magnetic phase diagram in terms of layer thicknesses. The validity of the one-dimensional assumption for the perpendicular situation is demonstrated. The phase diagram provides information on the type of demagnetization processes and the critical fields at which nucleation and reversal take place, depending on the intrinsic properties of the chosen soft and hard materials. An analytical expression of the reversal field is deduced for relatively large thicknesses. Moreover, the effect of a reduced interlayer coupling is also taken into account, leading to slight modifications of both the magnetic phase diagram and the hysteresis loops. A series of Fe/FePt bilayers, prepared by sputtering, has been used to evaluate the predictions of the model, which has also been tested with the available literature data on FeRh/FePt bilayers. Both systems have a particular relevance for potential applications in magnetic recording as well as magnetic microelectromechanical systems.

DOI: 10.1103/PhysRevB.73.094406 PACS number(s): 75.60.Jk, 75.60.Ej, 75.70.Cn, 75.50.Ss

I. INTRODUCTION

The concept of composite magnetic material has been revived in recent years mainly for the possible realization of *exchange-spring* magnets, that is, systems in which a soft and a hard magnetic phase are exchange coupled on a nanometric scale.[1] A variety of theoretical and experimental investigations reported in the literature have evidenced the inherent potential of this approach but they have also stressed the difficulties still existing as far as the technological side is concerned.[2] The synergic combination of a high-saturation-magnetization material and a high-anisotropy material has been specifically analyzed in the case of planar structures, as examples of highly oriented systems.[3] In particular, hard/soft bilayers and multilayers have been realized by various techniques with the aim of achieving planar permanent magnets with large energy product.[2] In principle, the choice of a hard layer with very high anisotropy enables the obtainment of both *parallel* and *perpendicular* exchange-spring systems, depending on the preferential direction of the hard layer magnetization with respect to the film plane. It is worth noticing that the *perpendicular* hard/soft exchange-spring system has recently found a possible application in the field of information storage.[4,5] The research on ultrahigh density magnetic recording is currently focused on the increase of magnetic anisotropy to avoid the thermostability problem, which is intrinsic to the increasingly smaller grain size. Unfortunately, the use of high perpendicular-anisotropy materials requires very intense applied fields for switching the information bits. A proposed solution for this drawback is the adoption of the heat-assisted magnetic recording (HAMR) or thermally assisted recording (TAR) technique,[6] applied to the exchange-spring system FeRh/FePt, in which FeRh is a soft meta-magnetic material.[4,5] As a further solution, it has been recently proposed[7] the exchange-spring trilayer FePt/Fe_3Pt/FePt, in which the Fe_3Pt represents the soft phase coupled to the hard FePt layers.[8]

An additional application of hard/soft exchange-spring magnets can be envisaged in the field of microelectromechanical systems (MEMS), where the performance of present microactuators is limited by the general application of electrostatic concepts.[9,10] In fact, the possible use of hard magnetic materials in MEMS microactuators (magnetic microactuators and systems, MagMAS) could enable the achievement of high acting forces under low voltage and large actuation displacements.[11] It is of particular interest in this respect the realization of *perpendicular* hard/soft exchange-spring magnets that could find application in MagMAS devices with perpendicular-design, an example of which is reported in Ref. 12. An important issue which is common to all the above-mentioned exchange-coupled systems concerns the description of the demagnetization processes and the capability of tailoring the magnetic properties of composite systems on the basis of the extrinsic (thickness, orientation) and intrinsic (anisotropy, magnetization, exchange) characteristics of the combined phases. The distinctive behavior of hard/soft exchange-spring systems is that they show a two-stage magnetization reversal, beginning at definite critical fields, the nucleation field H_{c1}, at which the magnetic moments start to depart reversibly and nonuniformly from the easy direction and the reversal field H_{c2} that puts forward the irreversible rotation of the whole system. We have recently developed a one-dimensional micromagnetic analysis of exchange-spring multilayers that endows

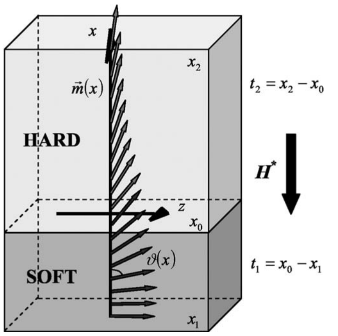

FIG. 1. Basic scheme for the one-dimensional continuum micromagnetic model of the hard/soft multilayer with anisotropy-axis perpendicular to the film plane.

with a detailed description of the magnetization reversal process, in the case of planar-anisotropy systems[2,3] (easy magnetization direction in the film plane). In the present work we will discuss an extension of our model to include the case of a hard phase with perpendicular anisotropy. Applying a magnetic field perpendicular to the film plane, a nonuniform magnetization distribution results due to the competition between the perpendicular anisotropy of the hard phase and the in-plane shape anisotropy of both phases. This particular distribution (named *perpendicular exchange spring*)[14] drives the switching process of the whole system. A crucial point in this subject concerns the demonstration, made in the present work, of the validity of the one-dimensional assumption for the perpendicular situation. The model has also been applied to the case of external magnetic field parallel to the film plane.

In order to verify the predictions of the model, we realized a series of Fe/FePt bilayers with perpendicular orientation of the hard phase and layers thickness in the range of a few nanometers.

A complete magnetic phase diagram of the Fe/FePt system is obtained and the dependence of the nucleation field on the layer thickness is calculated and compared to the experimental results. Complete hysteresis loops are also achieved by numerical calculations. The theoretical treatment is also extended considering the effect of a reduced interlayer exchange coupling with respect to the strong coupling assumption previously adopted. To this purpose we follow the same representation for the interlayer exchange coupling introduced by Guslienko *et al.*[14] and Garcia-Sanchez *et al.*[15] However we admit in our model a nonuniform magnetization distribution of the hard layer and finite magnetocrystalline anisotropy for the soft phase. Our results are acquired entirely on the basis of numerical evaluation of the obtained analytical expressions. A comparison is made with the model of Guslienko *et al.*[14] through the application to the FeRh/FePt bilayer system.

The paper is organized as follows. A description of the adopted micromagnetic model for the cases of perpendicular anisotropy and strong interlayer coupling is the content of Sec. II A. The effect of a reduced interlayer coupling is analyzed in Sec. II B. Section III reports the application of the model to the case of Fe/FePt bilayers. The experimental results on the latter system and the comparison with the theoretical predictions are exposed in Sec. IV. Finally the application of the model to the FeRh/FePt bilayer is considered in Sec. V.

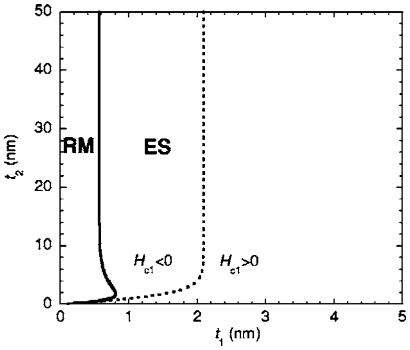

FIG. 2. Magnetic phase diagram in the plane of layer thicknesses t_1 (soft) and t_2 (hard) for a Fe/FePt bilayer with perpendicular anisotropy and the parameters reported in Sec. III. The figure reports the critical χ_∞ line ($\chi_c \rightarrow \infty$, full line) together with the isofield line corresponding to $H_{c1}=0$ (dashed line). **RM**=rigid magnet; **ES**=exchange-spring magnet.

II. THE MICROMAGNETIC MODEL

Hereafter we will describe the mathematical procedure utilized in our micromagnetic analysis for perpendicular magnetic anisotropy, with the field applied perpendicular to the film plane, for the cases of strong and reduced interlayer exchange coupling. The model is based on the continuum approximation and this implies that it should become inadequate when the layer thicknesses are comparable with the interatomic distance.[3] However, the comparison with the results of discrete one-dimensional models for the case of planar anisotropy[13] shows that the micromagnetic approach well represents the real system, down to thickness of a few atomic layers.

A. The case of strong interlayer exchange coupling

In the adopted model the following assumptions have been made:

1. The (infinite) *exchange-spring* multilayer is supposed to be made of alternate soft and hard layers perpendicular to the x axis (see the scheme in Fig. 1).
2. The two component layers are assumed to have uniaxial anisotropy with symmetry axes both perpendicular to the film plane, along the x axis (Fig. 1).
3. Only periodical solutions are considered, so that the median planes of the layers are symmetry planes for the magnetic structure.
4. The magnetization is uniform on each plane of the system, that is, no magnetic domains are present in the film plane.
5. The magnetization $\mathbf{M}_i$ in both hard and soft layers stay in the xz plane and the angles ϑ_i represent the orientation angle of $\mathbf{M}_i$ with respect to the x axis. This implies that the problem has a one-dimensional character so that the case of perpendicular anisotropy can be solved with the same math-

ematical treatment reported in Ref. 13. The detailed demonstration of the validity of the above assumption is reported in Appendix A.

6. A "strong" interlayer exchange coupling[16] is considered.

On the basis of the model we calculate the analytical expression of the differential susceptibility (χ_c) at the critical field H_{c1} (hereafter called *nucleation field*, as usual in the micromagnetic treatment)[17] that corresponds to the start of magnetization deviation from the saturated state.

Compared to the planar-anisotropy case, the perpendicular anisotropy requires the introduction of a further energy contribution, due to stray fields, in form of a demagnetizing anisotropy constant for each layer ($K_i^{dm}=-\mu_0 M_i^2/2$). With reference to Fig. 1 the magnetic field **H** is applied along the x axis (hence we will consider hereafter the *opposing* field $\mathbf{H}^*$ as a positive external field when it is applied along the negative x direction). In addition the total anisotropy constants $L_i=K_i-\mu_0 M_i^2/2$ replace the intrinsic anisotropy constants K_i considered in Ref. 13, assuming that positive K_i correspond to an intrinsic easy-axis parallel to the x axis. As usual in the literature, we consider the anisotropy constants K_i as effective values including volume, surface, and/or interface contributions.[2]

The expression of the Gibbs free energy density for a film portion with unitary area is

$$G=\sum_{i=1,2}(-1)^i\int_{x_0}^{x_i} F_i dx, \quad F_i=A_i\left(\frac{d\vartheta}{dx}\right)^2+\mu_0 M_i H^*\cos\vartheta+L_i\sin^2\vartheta, \tag{1}$$

where indexes 1 and 2 refer to the soft- and hard-layers, respectively, and x_0, x_1, and x_2 designate the position of the interface and of two contiguous median planes (Fig. 1); $\vartheta(x)$ is the angle between the magnetization vector **M** and the positive direction of x axis; A_i is the exchange stiffness constant of layer i. The intrinsic anisotropy contribution is limited to the second-order term with the condition that the anisotropy constant of the hard phase must be $K_2>|K_2^{dm}|$, so that L_2 turns out to be positive. On the contrary there is no limitation in principle to the sign of L_1: A negative value of this constant implies that the soft-phase easy direction is at $\pi/2$ with respect to that of the hard phase, which is parallel to $\mathbf{H}^*$ (see Ref. 18 for a detailed discussion on this point). This circumstance acquires a sound physical connotation in the case of perpendicular anisotropy, where a negative contribution to the total anisotropy necessarily comes from the local stray field. It is worth noting that the case $L_1>0$ is treated exactly as in Ref. 13.

The model can also be applied to the case of a bilayer and a symmetric trilayer system (hard/soft/hard). In the case of a multilayer the quantities $t_1=(x_0-x_1)$, $t_2=(x_2-x_0)$ represent half of the respective layer thicknesses. For the case of a bilayer t_1 and t_2 denote the whole hard- and soft-layer thicknesses, while for a hard/soft/hard trilayer the t_1 and t_2 parameters have the meaning of the soft-layer half thickness and of the hard-layer whole thickness, respectively.

The "strong" interlayer exchange coupling[16] implies the validity of the continuity condition, like as within the soft and hard layers

$$\vartheta(x_{o^-})=\vartheta(x_{o^+})=\vartheta_0. \tag{2}$$

The minimization of expression (1) leads to the so-called Euler equations

$$\frac{d^2\vartheta}{dx^2}+\left(\frac{\mu_0 M_i H^*}{2A_i}-\frac{L_i}{A_i}\cos\vartheta\right)\sin\vartheta=0 \quad (i=1,2), \tag{3}$$

with the boundary conditions (representing a particular case of the Weierstrass-Erdmann conditions of the variational calculus)

$$\left.\frac{d\vartheta}{dx}\right|_{x_1}=0, \quad \left.\frac{d\vartheta}{dx}\right|_{x_2}=0, \quad A_1\left.\frac{d\vartheta}{dx}\right|_{x_{0^-}}=A_2\left.\frac{d\vartheta}{dx}\right|_{x_{0^+}}, \tag{4}$$

where $i=1$ for $x_1<x<x_0$ and $i=2$ for $x_0<x<x_2$.

Because we are interested in the behavior for small angular deviations around the field H_{c1}^*, Eqs. (3) are expanded to the first order in ϑ. The obtained equations are then integrated between the extrema. We obtain a system of homogeneous linear equations at $H^*=H_{c1}^*$, leading to an implicit equation for the critical field H_{c1}^* (Ref. 3, 13, and 19)

$$A_1\gamma_1\tan(t_1\gamma_1)=A_2\gamma_2\tanh(t_2\gamma_2), \tag{5}$$

where

$$\gamma_i=\sqrt{(-1)^i\left(\beta_i-\frac{\alpha_i}{2}\right)},$$

and

$$\alpha_i=\frac{\mu_0 M_i}{A_i}H^* \text{ and } \beta_i=\frac{L_i}{A_i}.$$

From Eq. (5) one can easily demonstrate that, independently of layers' thickness

$$\frac{2L_1}{\mu_0 M_1}\leqslant H_{c1}^*\leqslant\frac{2L_2}{\mu_0 M_2}.$$

After differentiation of Eq. (5), one may verify that the quantity $\gamma_2 t_2$ always increases toward infinity by increasing t_2; hence for large enough values of t_2 we assume: $\tanh(t_2\gamma_2)\cong 1$ and Eq. (5) can be approximated by the following relation:

$$t_1\cong\frac{1}{\gamma_1}\tan^{-1}\frac{A_2\gamma_2}{A_1\gamma_1}, \tag{6}$$

which is independent of the hard-layer thickness t_2.

By expanding Eqs. (3) to higher orders in ϑ, an expression of the slope of $M(H^*)$ at the nucleation field H_{c1}^* is obtained so that the volume susceptibility at the critical field H_{c1}^* (in SI units), defined as $\chi_c=-dM/dH^*$, turns out to be

$$\chi_c = \left\{ \frac{M_1\left[\dfrac{t_1}{\cos^2(t_1\gamma_1)} + \dfrac{\tan(t_1\gamma_1)}{\gamma_1}\right] + M_2\left[\dfrac{t_2}{\cosh^2(t_2\gamma_2)} + \dfrac{\tanh(t_2\gamma_2)}{\gamma_2}\right]}{\dfrac{3p_1}{\cos^2(t_1\gamma_1)}\left[\dfrac{2t_1\gamma_1}{\sin(2t_1\gamma_1)} + 1\right] - \dfrac{3p_2}{\cosh^2(t_2\gamma_2)}\left[\dfrac{2t_2\gamma_2}{\sinh(2t_2\gamma_2)} + 1\right] + 2(p_1 - p_2)} \right\} \times \left\{ \alpha_1\left[\frac{1}{\gamma_1^2} + \frac{2t_1}{\gamma_1 \sin(2t_1\gamma_1)}\right] + \alpha_2\left[\frac{1}{\gamma_2^2} + \frac{2t_2}{\gamma_2 \sinh(2t_2\gamma_2)}\right]\right\}\left[\frac{1}{4H_{c1}^{*}(t_1 + t_2)}\right], \tag{7}$$

where

$$p_i = \frac{\alpha_i - 8\beta_i}{12(\alpha_i - 2\beta_i)} \quad (i = 1,2).$$

This expression is coincident with that obtained in Ref. 13.

The dependence of χ_c on the structural parameters allows us to define a phase diagram in the (t_1, t_2) plane. An example of the phase diagram is shown in Fig. 2 for a Fe/FePt system with perpendicular anisotropy of the hard FePt layer (see Sec. III A).

The critical susceptibility χ_c diverges along a critical line ($\chi_c \to \infty$), which corresponds to the onset of instability. This critical condition separates the exchange-spring (ES) regime ($\chi_c > 0$) from the rigid composite magnet (RM) one ($\chi_c < 0$). Physically the latter condition means that the equilibrium magnetization curve represents states of unstable equilibrium, so that the magnetization reversal occurs by an irreversible process starting directly from the saturated state. Thus in the RM regime the reversible portion of the demagnetization curve for $H < H_{c1} = -H_{c1}^{*}$ does not exist, differently from the ES regime.[13]

As described in details in Ref. 13, the critical line $\chi_c \to \infty$ (denoted in this paper as χ_∞) in the case of positive L_1 is typically U shaped with two vertical asymptotes.[13] It is possible to generalize the discussion given in Ref. 13 and to justify the presence of vertical asymptotes in the phase diagrams. The χ_∞ curve of the phase diagram is indeed obtained by imposing the vanishing of denominator in expression (7). If we suppose the existence of a nonhorizontal asymptote, its equation can be obtained by applying to the denominator of expression (7) the same approximation utilized in deducing Eq. (6)

$$p_1\left\{\frac{3}{\cos^2(t_1\gamma_1)}\left[1 + \frac{2t_1\gamma_1}{\sin(2t_1\gamma_1)}\right] + 2\right\} \cong 2p_2. \tag{8}$$

The combined Eqs. (6) and (8) form a system of equations in the variables t_1 and H_{c1}, and the χ_∞ curve of the phase diagram presents nonhorizontal asymptotes if (and only if) the system of equations admits solutions. Moreover, due to the fact that Eqs. (6) and (8) are independent of t_2, the asymptotes must be necessarily vertical. In general, the system of equations can admit many solutions, because it is nonlinear: Therefore the phase diagram could in principle present more than one vertical asymptote.

If the nucleation field H_{c1}^{*} marks the point at which the soft phase starts to deviate non-uniformly from the saturated state, a second critical field exists, i.e., the reversal field H_{c2}^{*}, at which the hard phase becomes unstable giving rise to the switching of the whole system. According to the model, the determination of H_{c2}^{*} is based on a criterion of instability of inhomogeneous rotation processes and the obtained values should be intended as an upper limit for the real reversal field, similar to the switching field of the Stoner-Wohlfarth model with respect to the coercivity of real bulk magnets. In general H_{c2}^{*} is determined through the numerical calculation of the demagnetization curve of the considered system. However, in the same way as in the case of planar anisotropy,[13] H_{c2}^{*} can be analytically determined in the limit of infinite thickness of the layers, t_1 and t_2 [Eq. (12) of the "depinning field" in Ref. 13]. In this case the demagnetization process starts from the soft phase, which undergoes a uniform reversible rotation until the irreversible switching of the hard phase occurs, in a way similar to a sudden penetration of a pinned domain wall. The magnetization orientation angles, at infinite distance from the interface, satisfy the equilibrium conditions of the individual soft and hard phases

$$\cos\vartheta_1 = \frac{\mu_0 M_1 H^{*}}{2L_1}, \quad \cos\vartheta_2 = \pm 1.$$

Therefore the condition at the interface [see Eq. (4)]

$$A_1 \left.\frac{d\vartheta}{dx}\right|_{\vartheta_{0^-}} = A_2 \left.\frac{d\vartheta}{dx}\right|_{\vartheta_{0^+}}$$

provides a relation between the applied magnetic field H^{*} and the angle ϑ_0. The instability condition for determining the critical field H_{c2}^{*} is $d\vartheta_0/dH^{*} \to \infty$, from which we obtain

$$H^*_{c2,dw} = \frac{2}{\mu_0} \frac{\left[M_1 L_2 + M_2 L_1 \left(\sqrt{1 - \frac{L_2 A_2}{L_1 A_1}} - 1 \right) \right] \sqrt{(L_1 A_1 - L_2 A_2) L_1 A_1}}{M_1^2 A_1 L_2 - (2 M_1 A_1 - M_2 A_2) M_2 L_1}, \quad (L_1 < 0). \tag{9}$$

Because of high effective anisotropy of both phases, L_1 and L_2 (in the soft phase the shape anisotropy is normally dominant), the variation of magnetization orientation is confined within narrow regions, of the order of the exchange lengths, around the interface [see Fig. 3(b)]. For this reason, even for layers thicknesses of only a few exchange lengths, H^*_{c2} approaches the asymptotic value given by Eq. (9) [see Figs. 4(b) and 5]. The described treatment can be developed also in the case of a magnetic field applied perpendicularly to the anisotropy axis of the hard layer, that is, parallel to the film surface (z axis). Also in this situation, it is possible to verify the validity of the one-dimensional assumption. Starting from saturation, the demagnetizing process occurs indeed following the one-dimensional solution. However, when the applied field crosses zero the configuration of magnetic moments becomes unstable and the azimuthal angle suddenly jumps from 0 to π. The final state of the system after this change is the symmetric one with respect to the x-y plane and a further increase of the applied field leads to saturation in the opposite direction. The detailed treatment of this case will be reported elsewhere.[20]

B. The case of a reduced interlayer exchange coupling

In previous paragraphs we supposed a "strong" coupling[16] occurring at the hard/soft interface, as represented by the continuity relation (2). Nevertheless the real systems may present a reduced coupling. In general, from a microscopic point of view we may presume, following Guslienko *et al.*,[14] that at the interface each atom of a given phase interacts with the (nearest neighbor) atom of the facing atomic plane belonging to the other phase, as schematically illustrated in Fig. 6. The corresponding exchange energy is

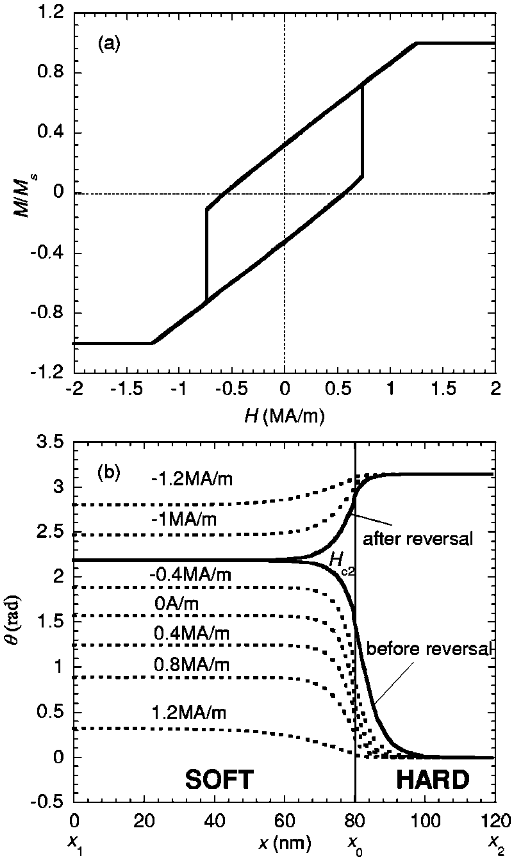

FIG. 3. (a) Major hysteresis loop for a FeRh/FePt bilayer with the parameters considered in Fig. 16, calculated assuming an interlayer coupling constant J_s with the same value of bulk coupling. (b) Behavior of the $\vartheta(x)$ function in correspondence to different magnetic field values along the hysteresis loop.

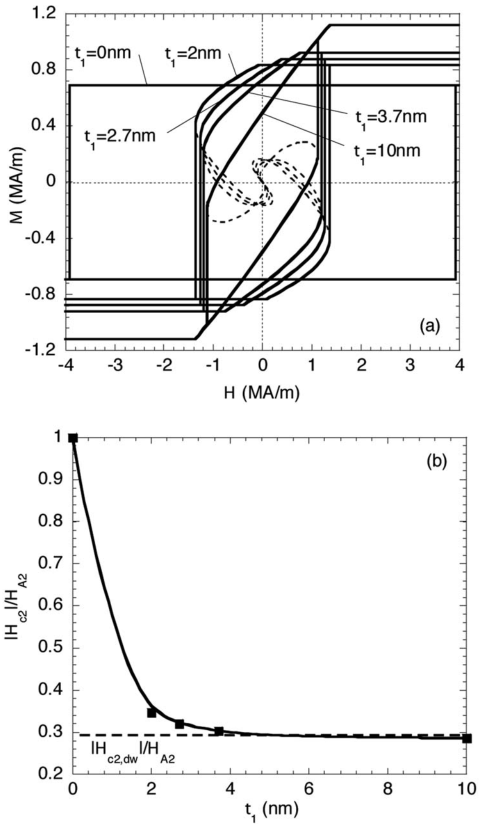

FIG. 4. (a) Calculated major hysteresis loops of the single layer FePt and of the Fe(t_1 nm)/FePt(10 nm) bilayers (with the parameters reported in Sec. III): The dashed lines correspond to the unstable portion of the equilibrium curves. (b) The soft-thickness dependence of the reversal field H_{c2} [full line: t_2 fixed to 10 nm; dashed line: $(t_1, t_2) \to \infty$], normalized to the hard-phase anisotropy field $H_{A2} = 2L_2/(\mu_0 M_2)$.

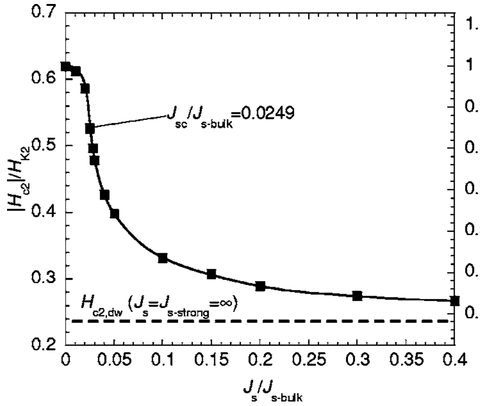

FIG. 5. Reversal field H_{c2} of the FeRh/FePt bilayer considered in Fig. 16 as a function of the interlayer coupling constant J_s (squares and full line). The reversal field is normalized to the magnetocrystalline anisotropy field of the hard layer $H_{k2}=2K_2(\mu_0 M_2)$ (left scale) and to the effective anisotropy field of the hard layer $H_{A2}=2L_2/(\mu_0 M_2)$ (right scale), while the J_s constant is normalized to the interlayer exchange constant of bulk phases $J_{s\text{-bulk}}$ [see Eq. (11)]. A particular point is evidenced on the curve, corresponding to the critical value J_{sc}, below which the curve is calculated by means of Eq. (17) (see text for further details). The dashed line represents the behavior of $H_{c2,\mathrm{dw}}$ as obtained in the case of "strong" coupling and infinite thickness of both layers [see Eq. (9)].

$$g_{\mathrm{ex}} = -I\vec{S}_1 \cdot \vec{S}_2 = -IS_1S_2\vec{m}_1 \cdot \vec{m}_2 = -J_s\vec{m}_1 \cdot \vec{m}_2,$$

where I represents the exchange integral, $\vec{S}_i$ are the spin vectors of the atoms, $\vec{m}_i=\vec{M}_i/M_i$ the magnetization unit vectors and J_s is a constant.

From the above definition we deduce the energy density per unit surface area at the interface (where a is the interatomic distance on a specific atomic plane)

$$G_s = \frac{g_{\mathrm{ex}}}{a^2} = -\frac{J_s}{a^2}\vec{m}_1 \cdot \vec{m}_2 = -J_{12}\mu_0\vec{M}_1 \cdot \vec{M}_2, \tag{10}$$

where

$$J_{12} = \frac{J_s}{a^2\mu_0 M_1 M_2}$$

has the same meaning as in Ref. 14. To estimate the order of magnitude of the constant J_s we take advantage of the fact that Eq. (10) may be utilized also to express the exchange energy density per unit volume within the bulk of a given phase, provided that the magnetization is uniform over (atomic) planes parallel to the film

$$F_{\mathrm{ex}} = \frac{J_s}{ca^2}(1-\vec{m}_1 \cdot \vec{m}_2),$$

where c is the distance between nearest neighbor atoms of different atomic planes, within a given phase or between the two layers at the interface, as in Fig. 6. In the above expression the arbitrary additive constant is chosen so that F_{ex} becomes zero when $\vec{m}_1$ and $\vec{m}_2$ are parallel.

By utilizing the standard derivation of the exchange energy density, we deduce

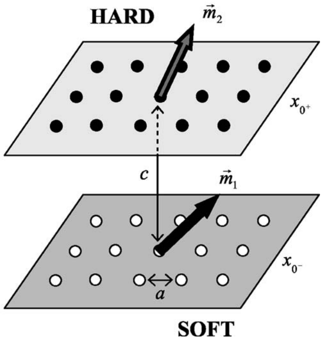

FIG. 6. Scheme of the interface region between the hard and soft layers, showing the two facing atomic planes.

$$J_s = J_{s\text{-bulk}} = \frac{2a^2A}{c}. \tag{11}$$

If we consider typical A values of the order of 10^{-12} to 10^{-10} J/m and $a \approx c \approx 10^{-10}$ m, from expression (11) we obtain J_s values of the order of 10^{-22} to 10^{-20} J (Ref. 14).

The Gibbs free energy for a film portion with unitary area becomes

$$G = \left(\sum_{i=1,2}(-1)^i\int_{x_0}^{x_i}F_i dx\right) + G_s = \left(\sum_{i=1,2}(-1)^i\int_{x_0}^{x_i}F_i dx\right) - J_{12}\mu_0 M_1 M_2(\vec{m}_1 \cdot \vec{m}_2 - 1), \tag{12}$$

where F_i is given by expression (1). Even in this case, one may verify the validity of the one-dimensional assumption and that the equilibrium configurations are solutions of the Euler equations

$$\frac{d^2\vartheta}{dx^2} + \left(\frac{\mu_0 M_i H^*}{2A_i} - \frac{L_i}{A_i}\cos\vartheta\right)\sin\vartheta = 0 \quad (i=1,2), \tag{13}$$

with boundary conditions

$$\left.\frac{d\vartheta}{dx}\right|_{x_1} = 0, \quad \left.\frac{d\vartheta}{dx}\right|_{x_2} = 0, \quad A_1\left.\frac{d\vartheta}{dx}\right|_{x_{0^-}} = A_2\left.\frac{d\vartheta}{dx}\right|_{x_{0^+}} = \nu\sin(\vartheta_{0^+} - \vartheta_{0^-}), \tag{14}$$

where

$$\nu = \frac{1}{2}J_{12}\mu_0 M_1 M_2.$$

These relations have to be compared with the corresponding Eqs. (3) and (4) and require the following constraints on the derivatives at the interface:

$$\left|\left.\frac{d\vartheta}{dx}\right|_{x_{0^-}}\right| \leqslant \frac{\nu}{A_1}; \quad \left|\left.\frac{d\vartheta}{dx}\right|_{x_{0^+}}\right| \leqslant \frac{\nu}{A_2}. \tag{15}$$

It has to be remarked that the boundary conditions (14) reduce to those obtained in the case of "strong" coupling when $\nu \to \infty$.

By developing the calculations in analogy with treatment reported in Ref. 13, we infer the implicit equation for the nucleation field H_{c1}^{*}

$$A_1\gamma_1 \tan(\gamma_1 t_1) = \frac{A_2\gamma_2 \tanh(\gamma_2 t_2)}{1 + \frac{1}{\nu}A_2\gamma_2 \tanh(\gamma_2 t_2)}. \tag{16}$$

Equation (16) reduces to Eq. (5) in the case of "strong" interface coupling ($\nu \to \infty$). In the case of absence of coupling ($\nu \to 0$) Eq. (16) becomes

$$\tan(\gamma_1 t_1) = 0,$$

independent of the hard-layer thickness t_2. The solution is

$$H_{c1}^{*} = \frac{2L_1}{\mu_0 M_1}$$

corresponding to a positive nucleation field $H_{c1} = -H_{c1}^{*}$ only due to the soft phase. In this case, the two layers are decoupled magnetic systems, characterized by different interface boundary conditions.

It is interesting to notice that, starting from the decoupled state and gradually increasing the value of coupling constant J_s, the system goes progressively away from the decoupled state evidencing the occurrence of a novel critical field H_{c12}. When decreasing the applied field, this critical field corresponds to a complete reversal of the soft-layer magnetization, while the hard-layer maintains its initial saturation state. We can individuate the critical field H_{c12} by solving the Euler equations to the first order in ϑ for the hard layer and to the first order in $\psi = \pi - \vartheta$ for the soft layer. The implicit equation for the critical field H_{c12} turns out to be

$$A_1\gamma_1 \tanh(\gamma_1 t_1) A_2\gamma_2 \tanh(\gamma_2 t_2) = \nu[A_1\gamma_1 \tanh(\gamma_1 t_1) + A_2\gamma_2 \tanh(\gamma_2 t_2)] \tag{17}$$

where

$$\gamma_1 = \sqrt{\frac{\alpha_1}{2} + \beta_1}, \quad \gamma_2 = \sqrt{\beta_2 - \frac{\alpha_2}{2}}.$$

Equation (17), for small enough ν values, admits two solutions lying between the extrema

$$H_{\min} = -H_{\max}^{*} = -\frac{2L_2}{\mu_0 M_2} \text{ and } H_{\max} = -H_{\min}^{*} = \frac{2L_1}{\mu_0 M_1},$$

which coincide with the solutions for the case $\nu \to 0$ of the decoupled system. The smallest (in absolute value) solution coincides with the critical field H_{c12}, while the largest one is the reversal field H_{c2} [see Fig. 7(a)]. On increasing ν values, the two solutions approach one another and become coincident for a given critical value ν_c, corresponding to a critical value J_{sc} of the exchange coupling constant. For larger ν values Eq. (17) has no more solutions. However, when ν is larger than the critical value ν_c, a reversal field H_{c2} still exists, but it can not be deduced by means of an implicit equation like Eq. (17).

Coming back to the nucleation field H_{c1}^{*}, we are able to achieve the expression of the volume susceptibility at this critical field (in SI units)

$$\chi_c^{\omega} = \left\{ \frac{M_1\left[\frac{t_1}{\cos^2(\gamma_1 t_1)} + \frac{1}{\gamma_1}\tan(\gamma_1 t_1)\right] + \omega^2 M_2\left[\frac{t_2}{\cosh^2(\gamma_2 t_2)} + \frac{1}{\gamma_{2cr}}\tanh(\gamma_2 t_2)\right]}{p_1\left\{\frac{3}{\cos^2(\gamma_1 t_1)}\left[1 + \frac{2\gamma_1 t_1}{\sin(2\gamma_1 t_1)}\right] + 2\right\} - \omega^3 p_2\left\{\frac{3}{\cosh^2(\gamma_2 t_2)}\left[\frac{2t_2\gamma_2}{\sinh(2\gamma_2 t_2)} + 1\right] + 2\right\}} \right\}$$
$$\times \left\{\alpha_1\left[\frac{1}{\gamma_1^2} + \frac{1}{\gamma_1}\frac{2t_1}{\sin(2\gamma_1 t_1)}\right] + \omega\alpha_2\left[\frac{1}{\gamma_2^2} + \frac{2t_2}{\gamma_2 \sinh(2\gamma_2 t_2)}\right]\right\}\frac{1}{4H_{c1}^{*}(t_1 + t_2)}, \tag{18}$$

where

$$\omega = \frac{1}{1 + \frac{1}{\nu}A_2\gamma_2 \tanh(\gamma_2 t_2)}$$

represents a positive quantity with $0 < \omega < 1$. For $\nu \to \infty$ and hence $\omega = 1$ we again obtain Eq. (7).

III. FE/FEPT BILAYER: MAGNETIC PHASE DIAGRAM AND HYSTERESIS LOOPS

We will now use our model to make predictions for Fe/FePt bilayers, with reference to a particular set of realized samples (see Sec. IV), for which Fe layers with thickness 2, 2.7, 3.7, and 10 nm were deposited over a 10 nm FePt layer. We will consider the following layer intrinsic parameters: $M_1 = 1.55$ MA/m, $K_1 = 0$ (from which: $L_1 = -1.5$ MJ/m^3), $M_2 = 0.69$ MA/m, $K_2 = 2$ MJ/m^3 (from which: $L_2 = 1.7$ MJ/m^3), $A_1 = A_2 = 10^{-11}$ J/m. For the choice of the values of M_1, M_2, and K_2 see discussion in Sec. IV. We will assume that the magnetocrystalline anisotropy of Fe is negligible.

A. Case of strong interlayer exchange coupling

Figure 2 represents the phase diagram of an exchange-spring bilayer of Fe/FePt. It has to be reminded that, in the

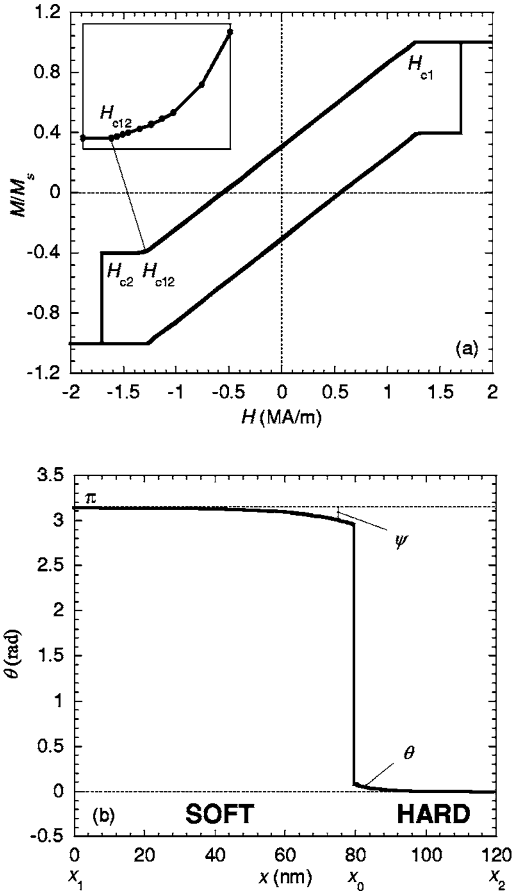

FIG. 7. (a) Major hysteresis loop for a FeRh/FePt bilayer with the parameters considered in Fig. 16, calculated assuming an interlayer exchange constant $J_s=0.02\times J_{s\text{-bulk}}$. Inset: enlarged-scale portion of the loop in the region close to the critical field H_{c12}. (b) Behavior of the $\vartheta(x)$ and the $\psi(x)=\pi-\vartheta(x)$ functions, corresponding to the magnetic field value $H=-H^{*}=-1.34$ MA/m (which is slightly below the critical field H_{c12}).

case of a bilayer, the t_1 and t_2 parameters represent the whole hard- and soft-layer thicknesses, respectively.

This case is an example of a system having the two phases with total anisotropy constant L_i of opposite sign and thus mutually perpendicular easy axes. In the phase diagram of Fig. 2, the critical line χ_∞ is no more U shaped as it is for a conventional planar exchange spring[13] and moreover it crosses the origin of coordinate axes. Nevertheless, we still distinguish the ES regime ($\chi_c>0$) from the RM one ($\chi_c<0$). Due to the high magnetostatic energy favoring the in-plane magnetization of the soft layer, the occurrence of the RM regime is expected at lower thickness of the soft layer (t_1), as compared to the planar anisotropy configuration.[13] No explicit decoupled magnet (DM) region is found in the perpendicular anisotropy case (see also the discussion at the end of Sec. II). However, the region of very large thicknesses (the limit of two bulk soft- and hard-phases coupled at the interface) behaves as an effectively decoupled system.

Another peculiarity of the diagram is that the critical field $H_{c1}=-H_{c1}^{*}$ admits both positive and negative values. In Fig. 2, the region $H_{c1}>0$ corresponds to nucleation fields in the first quadrant of the hysteresis loop. As a consequence, the ES region with negative nucleation fields occurs at low t_1 values.

TABLE I. Calculated values of the critical fields H_{c1} and H_{c2} for the perpendicular field configuration, in the case of a series of Fe(t_1 nm)/FePt(10 nm) bilayers.

t_1 (nm)	H_{c1} (MA/m)	H_{c2} (MA/m)
0	−3.92	−3.92
2	−0.08	−1.36
2.7	0.39	−1.26
3.7	0.77	−1.19
10	1.38	−1.12

The calculated values of the nucleation field H_{c1}^{*} for the FePt single layer and for the Fe/FePt bilayer are reported in Table I. The continuous line in Fig. 8 shows the soft layer thickness dependence of the nucleation field obtained from Eq. (5), with the hard-layer thickness fixed to $t_2=10$ nm.

The determination of the major hysteresis loops may be performed by numerically solving the Euler equations on the basis of the *shooting* method. In correspondence to every field value the problem admits in general more than one solution and this way allows identifying both the minimum energy (stable) solutions and the maximum energy (unstable) solutions. The magnetization per unit surface area of the bilayer is calculated as the mean magnetization in the field direction ($i=1,2$)

$$M=\frac{\sum_{i=1}^{2}\left[(-1)^{i}M_i\int_{x_0}^{x_i}\cos\vartheta dx\right]}{\sum_{i=1}^{2}t_i}.$$

Figure 4(a) reports a series of major hysteresis loops calculated for the single FePt layer and Fe/FePt bilayers with $t_1=2$, 2.7, 3.7, and 10 nm (and t_2 fixed to 10 nm). The calculated reversal fields of the bilayers are reported in Table I. In the loops of Fig. 4(a) we also trace the portions that refer to unstable equilibrium states, indicated as dashed lines, which are continuously connected with the stable states. In the

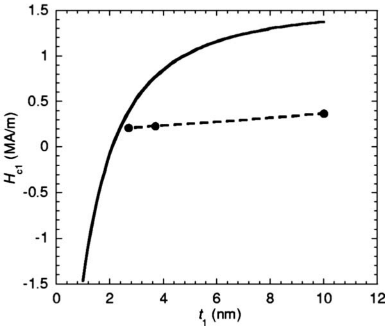

FIG. 8. Nucleation field H_{c1} of the Fe(t_1 nm)/FePt(10 nm) bilayers (with the parameters reported in Sec. III) as a function of the soft-layer thickness: theoretical curve (full line) and experimental points (the dashed line is a guide to the eyes).

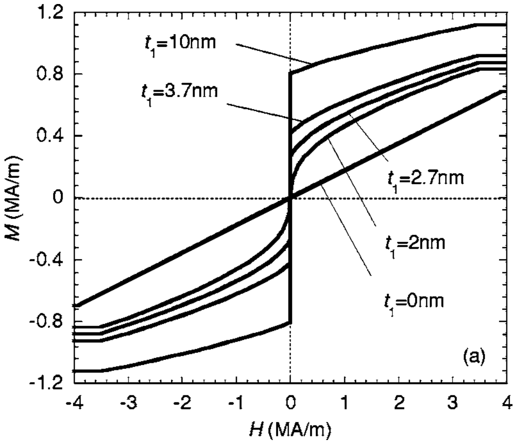

FIG. 9. Calculated major hysteresis loops of the single layer FePt and of the Fe(t_1 nm)/FePt(10 nm) bilayers (with the parameters reported in Sec. III). The magnetic field is applied parallel to the film plane.

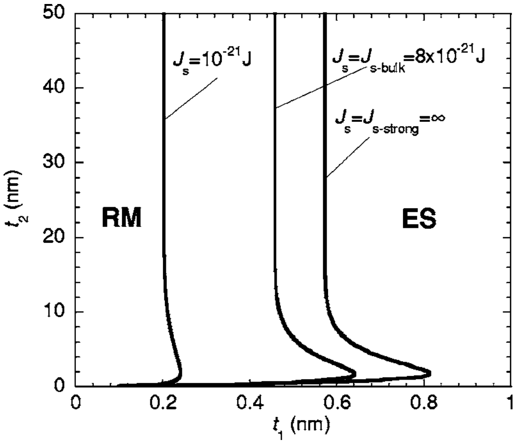

FIG. 10. Magnetic phase diagram in the plane of layer thicknesses t_1 (soft) and t_2 (hard) for the case of a Fe/FePt bilayer, with the parameters reported in Sec. III. The figure reports the critical χ_∞ line ($\chi_c \rightarrow \infty$) for three different values of the interlayer coupling J_s constant, having fixed a=0.4 nm (see text and Fig. 6).

present case, these lines are s-shaped curves that cross the origin (H^*=0, M=0), due to central symmetry.

The soft-thickness dependence of the reversal field H_{c2} (t_2 fixed to 10 nm) is then shown in Fig. 4(b), where the critical field values are normalized to the hard-phase anisotropy field $H_{A2}=2L_2/(\mu_0 M_2)$. Confirming what was stated in Sec. II we notice that this curve rapidly approaches an asymptotic value with increasing t_1. This value increases with the thickness t_2 of the hard layer and it turns out to be close to the limiting value $H_{c2,dw}=-H^*_{c2,dw}=-1.14$ MA/m given by Eq. (9) for $(t_1,t_2)\rightarrow\infty$.

Figure 9 shows the calculated hysteresis loops with the field applied in the film plane. The loop of the t_1=2 nm bilayer is completely reversible and does not show any discontinuity, while the loops of the bilayers with t_1=2.7, 3.7, and t_1=10 nm present a discontinuity at zero field and thus a nonzero remanence. This reflects the fact that at zero field the magnetization configuration defined by $\vartheta(x)$ is the same both in the case of parallel and perpendicular initial saturation. As an example, in the case t_1=2 nm the remanence state corresponds to the system in a saturated state along the x direction because the perpendicular nucleation field lies in the second quadrant [see Fig. 4(a)] and thus the z component of magnetization is zero. We notice that, for a fixed hard-layer thickness, the nucleation field becomes rapidly independent of the soft-layer thickness.

B. Case of a reduced interlayer exchange coupling

If we now consider a reduced interlayer coupling [Gibbs free energy (12)], the phase diagram (χ_∞ curve) of Fig. 2 is modified. In Fig. 10 the χ_∞ curves in the (t_1,t_2) plane are reported for the Fe/FePt bilayer, as calculated by Eq. (18), for three values of J_s (the intermediate value $J_s=J_{s\text{-bulk}}=8\times10^{-21}$ J corresponds to the bulk exchange constant $A_1=A_2$ of the two layers). The ES region is on the right of each curve and we can notice that, on decreasing the exchange coupling, the rigid magnet region (RM) of the phase diagram shrinks. In the case of the absence of coupling the bilayer always shows reversible behavior independently of the layers thicknesses and only due to the soft-phase magnetization reversal. Figure 11 shows the dependence of the nucleation field on J_s for different soft-layer thicknesses in the case of Fe/FePt bilayers. One may notice that the difference between the nucleation field corresponding to the bulk exchange constant and to the "strong" coupling case (horizontal dashed lines in Fig. 11) is vanishing on increasing the soft-layer thickness, while relevant effects occur in the case of very thin soft layers.

The determination of major hysteresis loops may be performed once more by numerically solving the Euler equations; but in this case we must utilize the following relations [deduced from Eqs. (14)] to link up the solutions of the soft and hard layers

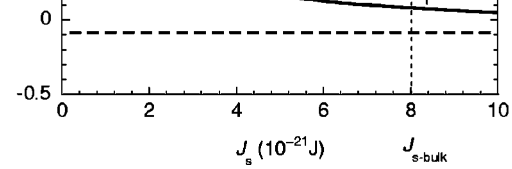

FIG. 11. Dependence of the nucleation field for the Fe(t_1 nm)/FePt(10 nm) bilayers (with the parameters reported in Sec. III) as a function of the interlayer coupling constant J_s, having fixed a=0.4 nm. The horizontal dashed lines refer to the ideal case $\nu\rightarrow\infty$ ("strong" coupling).

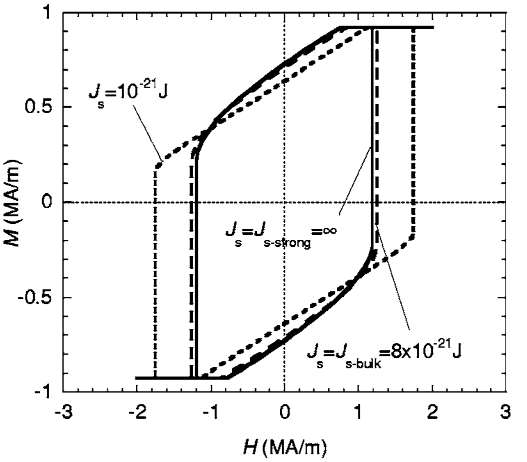

FIG. 12. Calculated major hysteresis loops for the Fe(3.7 nm)/FePt(10 nm) bilayer (with the parameters reported in Sec. III) for three different values of the interlayer coupling constant J_s, having fixed $a=0.4$ nm. The magnetic field is applied perpendicular to the film plane.

$$\vartheta_{0^+}=\arcsin\left(\frac{A_1}{\nu}\left.\frac{d\vartheta}{dx}\right|_{x_{0^-}}\right)+\vartheta_{0^-},\qquad \left.\frac{d\vartheta}{dx}\right|_{x_{0^+}}=\frac{A_1}{A_2}\left.\frac{d\vartheta}{dx}\right|_{x_{0^-}}$$

and take into account the constraints (15). The obtained hysteresis loops for the Fe/FePt bilayer are reported in Fig. 12 for $t_1=3.7$ nm and different J_s values. The plots show that when the interlayer coupling increases the remanence increases as well, while the reversal field decreases (in absolute value). In the limiting case of the absence of coupling, the reversal field tends to the anisotropy field of the hard phase $H_{A2}=2L_2/(\mu_0 M_2)$. Note that the hysteresis loops for the cases of "strong" and "bulk" interface coupling (see Sec. II B) are nearly coincident.

IV. FE/FEPT BILAYER: EXPERIMENTAL RESULTS

A. Experimental details

The properties of the hard phase were optimized by preparing FePt films of a nominal thickness of 10 nm on MgO(100) under several growth conditions. Suitable results in terms of (001) orientation, magnetic anisotropy, and squareness of the perpendicular loop were obtained by a process based on the rf-sputtering growth at 550 °C followed by post-annealing at the same temperature.[21] The growth was based on the alternate deposition of Fe and Pt layers of approximately 2 Å, in order to obtain the nominal composition $Fe_{53}Pt_{47}$, and it was realized under an Ar pressure of 1.4×10^{-2} mbar, with growth rates in the range 0.2–0.6 Å/s. The structural characterization, performed by x-ray diffraction and transmission electron microscopy, indicated that FePt grew epitaxially on MgO with perpendicular orientation of the [001] axes and with ordering parameter $S=0.93$.[21] From TEM observations the effective FePt film thickness turned out to be 9.25 nm and the FePt layer was found to be composed of interconnected grains having a 15–25 nm lateral size.[21] Under the same sputtering conditions, Fe layers with nominal thicknesses of 2, 2.7, 3.7, and 10 nm were deposited at room temperature on the FePt layer and covered by Pt or Ag overlayers. The x-ray reflectivity (XRR) experiments, performed on the Fe(3.7 nm)/FePt(10 nm) bilayer, gave important information on the morphology of the system. In order to refine the experimental XRR profile, some layers of intermediate electron density between Fe and FePt had to be introduced, in order to take into account both the granular morphology of the sample and the presence of an interdiffusion process between the layers. The evaluated fraction of unmixed Fe was 60% of its nominal value, i.e., approximately 2 nm. As regards the intermixing between Fe and the underlying FePt, we could conclude that the interdiffusion region is limited to 0.5–1 nm (Ref. 22).

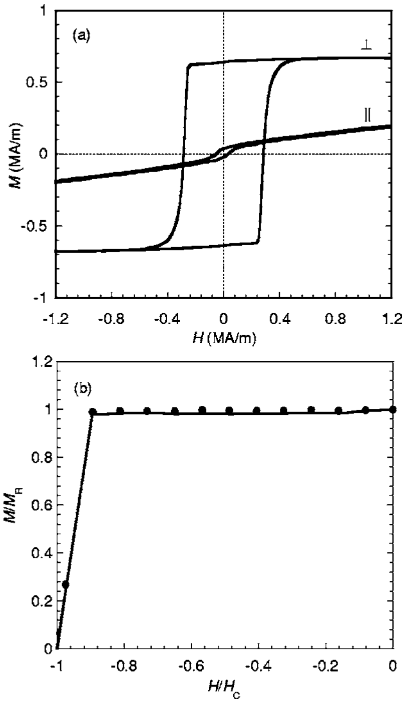

FIG. 13. (a) Experimental parallel and perpendicular hysteresis loops of the FePt film 10 nm thick; (b) dc-demagnetizing remanence (dots) compared with the second quadrant portion of the demagnetizing curve (full line) in the perpendicular field configuration.

The magnetic characterization (hysteresis loops, dc-demagnetization remanence[1]) was carried out by means of an alternating gradient force magnetometer (AGFM) and a superconducting quantum interference device (SQUID) magnetometer.

B. Magnetic characterization

The magnetic characteristics of the hard FePt layer fulfill the requirements of the model in terms of orientation and anisotropy energy. The hysteresis loops measured on the FePt film in the parallel and perpendicular configurations are shown in Fig. 13(a). Coherently with the structural results, the easy-magnetization direction is perpendicular to the film plane. The perpendicular loop has a high squareness (Sq $=0.93$), calculated as the area of the loop in the second quadrant divided by the product between remanence and coerciv-

TABLE II. Magnetic properties of the realized FePt film and of the Fe(t_1 nm)/FePt(10 nm) bilayers.

t_1 (nm)	$(M_r/M_s)_\perp$	$M_{s\perp}$ (MA/m)	$M_{r\parallel}/M_{s\perp}$	H_c (MA/m)	H_{c1} (MA/m)
0	0.96	0.690	0.05	−0.283	—
2	0.98	0.690	0.12	−0.283	—
2.7	0.79	0.700	0.09	−0.275	0.215
3.7	0.82	0.980	0.17	−0.271	0.231
10	0.37	0.820	0.39	−0.057	0.374

ity. As shown in Table II, the values of perpendicular coercivity ($H_{c\perp}$) and remanence ratio (M_r/M_s) are 0.283 MA/m and 0.96, respectively. The parallel remanence is only 5% of the perpendicular saturation magnetization ($M_{s\perp}$), possibly due to a residual fraction of soft phase, or to a small tilting of a fraction of c axes from the perpendicular direction.[21] The uniaxial effective anisotropy constant K, evaluated by extrapolating the parallel loop to M_s, is 2 MJ/m^3.

The magnetic behavior manifested by the Fe(t_1)/FePt(10 nm) bilayers suggests a varied phenomenology, where the thickness of the soft layer is the critical parameter. The parallel and perpendicular hysteresis loops measured for t_1=2, 2.7, 3.7, and 10 nm are reported in Figs. 14(a)–14(d). The dc-demagnetizing remanence of the FePt film and bilayer samples is also shown in the four panels of Figs. 15(a)–15(d), where it is compared with the second quadrant portion of the demagnetizing curve. For t_1=2 nm the perpendicular loop is square shaped and shows a remanence ratio higher than 0.9 (Table II). Moreover, the demagnetizing process is characterized by a single critical field, which, according to the demagnetizing remanence curve, corresponds to the start of the irreversible magnetization reversal. No gain in magnetization, as compared to the demagnetizing portion of the loop, is in fact obtained when measuring the demagnetizing remanence in the second quadrant, which is the behavior manifested by the hard layer [Fig. 13(b)].

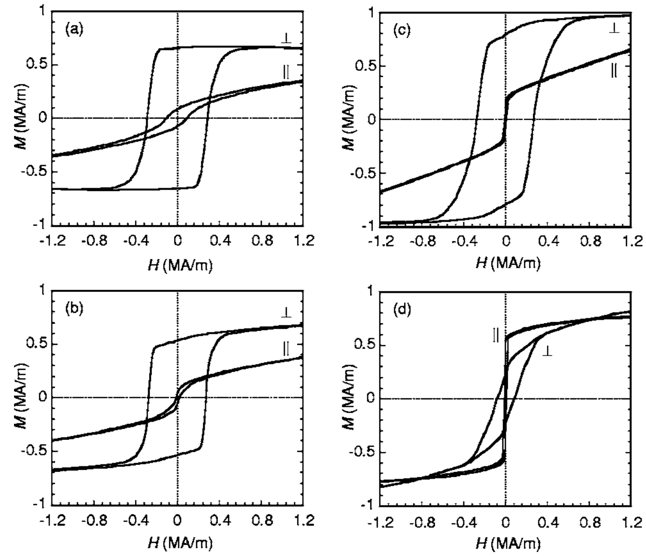

FIG. 14. Experimental parallel and perpendicular hysteresis loops of the Fe(t_1 nm)/FePt(10 nm) bilayers: (a) t_1=2 nm; (b) 2.7 nm; (c) 3.7 nm; and (d) 10 nm.

By increasing Fe thickness, the remanence ratio decreases ($M_r/M_s \cong 0.8$ for t_1=2.7, 3.7 nm and $M_r/M_s \cong 0.4$ for t_1 =10 nm), due to the start of the magnetization reversal at positive field values. The occurrence of a marked nucleation field in the first quadrant can be noticed in the perpendicular loops of the bilayers with higher Fe content. In the bilayer with t_1=2 nm, for which no definite kink is observed in the first quadrant, the demagnetizing remanence is clearly different from that of bilayers with t_1=2.7, 3.7, and 10 nm (see Fig. 15). The demagnetizing remanence of these bilayers is higher than the loop magnetization, indicating a reversible demagnetizing process down to fields close to coercivity. The thinnest bilayer behaves instead as a single magnetic phase (rigid magnet), giving a clear evidence of the existence of exchange coupling between soft and hard layers.

When considering the magnetic parameters of the bilayers (see Table II), we notice that the perpendicular coercivity is not substantially reduced compared with the FePt film by adding a Fe layer of thickness up to 3.7 nm.

Some attention has to be paid to the measured magnetization values, which are much lower in the FePt film compared

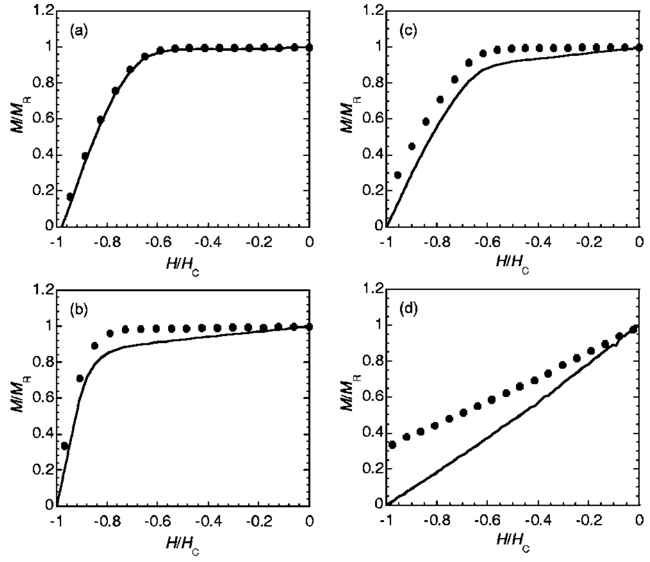

FIG. 15. dc-demagnetizing remanence of the Fe(t_1 nm)/FePt(10 nm) bilayers (dots), in the perpendicular configuration, compared with the second quadrant portion of the demagnetizing curve (full line): (a) t_1=2 nm; (b) 2.7 nm; (c) 3.7 nm; and (d) 10 nm.

TABLE III. Sensitivity of H_{c1} to the variation of different parameters in the case of a series of Fe(t_1 nm)/FePt(10 nm) bilayers. The sensitivity is expressed as the ratio between the relative uncertainty on H_{c1} and that on the parameters.

t_1 (nm)	$\frac{(\partial H_{c1}/\lvert H_{c1}\rvert)}{(\partial M_1/M_1)}$	$\frac{(\partial H_{c1}/\lvert H_{c1}\rvert)}{(\partial t_1/t_1)}$	$\frac{(\partial H_{c1}/\lvert H_{c1}\rvert)}{(\partial N_1/N_1)}$	$\frac{(\partial H_{c1}/\lvert H_{c1}\rvert)}{(\partial K_2/K_2)}$
2	33.8	21.3	16.5	−8.1
2.7	6.4	3.6	3.7	−1.0
3.7	2.9	1.3	1.9	−0.3
10	1.2	0.2	1.1	−0.02

to the bulk (0.69 against 1.14 MA/m, as in Ref. 23). The nonmonotonic increase of M_s with Fe thickness reflects the importance of the experimental uncertainties, depending on instrumental sensitivity, evaluation of the diamagnetic contribution of substrate and sample holder, and effective microstructure of the samples. The spread in the literature data on FePt films, going from 0.4 MA/m (Ref. 24) to 0.8 MA/m (Ref. 25), 1.0 MA/m (Refs. 26–28) and 1.1 MA/m (Refs. 29 and 30), underlines the difficulty in the determination of the M_s value.

The hysteresis loops measured with in-plane field (hard direction) are also reported in Fig. 13(a) (FePt film) and Fig. 14 (Fe/FePt bilayers). It can be underlined that the remanence measured in the in-plane loops of the bilayers is predicted by the model for $t_1 > 2$ nm (see Fig. 9). The small contribution of a residual parallel fraction, as observed in the FePt film, has also to be considered [Fig. 13(a)].

C. Comparison between experiments and results of the model

In Sec. III, the magnetic phase diagram and hysteresis behavior of Fe(t_1)/FePt(10 nm) bilayers are calculated as a function of the soft layer thickness t_1 based on the experimental parameters measured on the FePt(10 nm) film. In the calculation, the spontaneous magnetization $M_1 = 1.55$ MA/m of the soft Fe layer are evaluated by considering both our measurements on Fe films and literature data.[31] Moreover, the exchange-stiffness constant A of the Fe and FePt layers are both considered equal to 10^{-11} A/m. A first, qualitative agreement between theoretical and experimental results can be identified in the change from the RM to the ES regime with increasing the thickness of the soft layer. The bilayer with $t_1 = 2$ nm shows an apparent RM behavior with a single critical field at which the magnetization is irreversibly switched. For larger thickness of the soft layer (bilayers with $t_1 = 2.7$, 3.7, and 10 nm) the magnetization reversal starts at positive field values and the process is reversible down to fields close to coercivity (see Fig. 15). This is a clear indication of an exchange-spring (ES) character. The transition region between the two regimes has to be identified in the range between 2 and 2.7 nm, that is, at a larger soft-layer thickness compared to the calculated phase diagram, where the critical line is located below $t_1 = 1$ nm (Fig. 2). However, in the case of the bilayer with $t_1 = 2$ nm, a different possibility has to be taken into account, that is, the system could undergo a sudden switching of magnetization (due, for instance, to nucleation and propagation of domain walls, a phenomenon that is not considered by the model) for a critical field H_c before the theoretical H_{c1} is reached (ES with $|H_c| < |H_{c1}|$). In this way, the actual nature of ES could be masked and one cannot undoubtedly attribute the RM character to the system. Thus the transition boundary between the RM and ES regimes could only be identified in the region below 2.7 nm, that is, in a qualitative agreement with the calculated phase diagram.

In order to widen the quantitative comparison between model and experiments, we deduce the nucleation fields H_{c1} from the perpendicular hysteresis loops in Fig. 14. The obtained values are reported in Table II and compared in Fig. 8 with the results of the model. Unless the bilayer $t_1 = 2$ nm is ES with $|H_c| < |H_{c1}|$ (in such a case the nucleation field should be negative, as predicted by the model), in the investigated range of soft-layer thicknesses no negative values of the nucleation field are measured. Moreover the experimental positive values are lower than those predicted by the model.

A possible origin of quantitative disagreement can be found in the parameters used in the calculation, the estimation of which is not always straightforward. We evaluate the sensitivity of the calculated nucleation field H_{c1} with respect to the different parameters (t_i, M_i, K_i, A_i). As new parameters we add the demagnetizing factors N_i of the two phases, removing the simplistic hypothesis that our system behaves as a continuous film with infinite lateral extension ($N_i = 1$). As a matter of fact TEM analysis indicates that the FePt system is constituted of nanometric grains, thus supporting the hypothesis of a locally reduced demagnetizing factor. The same can be inferred for the soft layer, since also the bilayers are characterized by a granular morphology. These parameters are accounted for by considering effective anisotropy constants $L_i = K_i - \mu_0 N_i M_i^2/2$.

The evaluation of sensitivity is done by deducing the partial derivatives with respect to the parameters, starting from Eq. (5), and the results are reported in Table III for the Fe/FePt bilayer. It can be underlined that the largest sensitivity of H_{c1} is obtained for the variations of M_1 and N_1. The sensitivity of H_{c1} to the variation of the other parameters is negligible, except in the case of very thin Fe layers, for which also the changes of t_1 and M_2 are relevant.

Therefore we focus our attention on the parameters M_1 and N_1 and repeat the determination of H_{c1} on the basis of more realistic values. In particular an independent decrease of both parameters determines a shift of the calculated values of the nucleation field toward the experimental data.

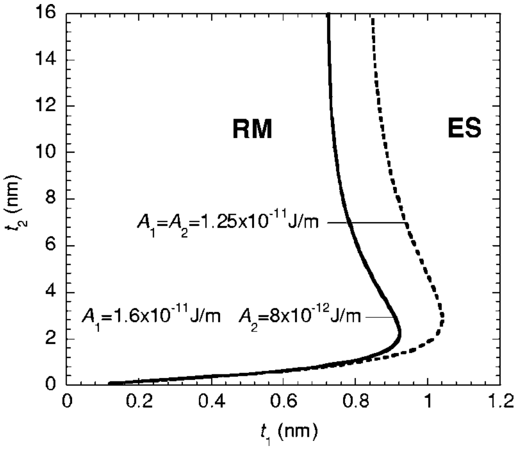

FIG. 16. Magnetic phase diagram in the plane of layer thicknesses t_1 (soft) and t_2 (hard) for the case of a FeRh/FePt bilayer, with parameters $M_1=1.27$ MA/m, $K_1=0$; $M_2=1.1$ MA/m, $K_2=2$ MJ/m^3. The reported χ_∞ lines refer to two different cases (see text): (a) $A_1=1.6\times10^{-11}$ J/m and $A_2=8\times10^{-12}$ J/m (full line); (b) $A_1=A_2=1.25\times10^{-11}$ J/m (dashed line).

We consider the possibility of a reduced magnetization M_1 for the soft layer, in order to keep into account the uncertainty in the evaluation of the Fe layer moment due to the intermixing with underlying (FePt) and overlying layer (Pt) and the possible presence of intergrains voids or wavy surfaces. As an example, in the case of Fe(10 nm)/FePt(10 nm) bilayer, combining magnetic and XRR measurements we deduce a saturation magnetization value of $M_1=1.0$ MA/m. For this sample the best agreement between experimental and theoretical nucleation field is obtained with $N_1=0.6$, a value which can be reasonably correlated to the specific microstructure of the bilayer. This can be considered a reliable approach since both the uncertainty in the experimental evaluation of M_1 and the theoretical sensitivity of H_{c1} to parameter M_1 are lower for $t_1=10$ nm sample than for the others. Conversely, even if a reduction of M_1 leads in general to a better correlation with experiments, the application of the above method to the samples with $t_1<10$ nm is less reliable.

For all the samples an improved agreement with experiments is obtained by fixing M_1 to 1.55 MA/m and selectively modifying the demagnetizing factor of the soft phase. The obtained values of N_1 turn out to be lower than unity (in the range 0.4–0.9) and likely correlated to the specific microstructure of the layers with different thicknesses.

As expected, the calculated critical fields H_{c2} (Table I) are systematically larger than the experimental coercive fields, reported in Table II. The field H_{c2} represents indeed the upper limit of the coercive field that in real systems is conditioned by the presence of domain walls nucleation and pinning (see discussion in Sec. II). Magnetic force microscopy (MFM) observations support this assumption showing the presence of intergrain magnetic domains.[32] Moreover, a peculiarity of our systems is that the coercivity is not substantially reduced in the bilayers compared to the hard layer (Table II), a reduction instead expected for exchange-coupled systems.

As for the effect of a reduced interlayer coupling on the magnetic behavior of Fe/FePt bilayers, the analysis of Sec. III B evidences, with respect to the "strong" coupling case, an increase of the H_{c1} values (reduction of hardness) that is more marked for the thinnest bilayers (Fig. 11). Due to the fact that the experimental nucleation fields are lower than the predicted values in the case of strong coupling, we have an indication that the reduction of interlayer coupling cannot explain such a discrepancy. As a result of this analysis we can infer that the realized systems possibly present an intense interface coupling. Recently, the occurrence of an intermixing at the interface, like that occurring in the present case, has been indeed claimed to represent an approach for improving exchange-spring magnets.[33]

The model predicts the correct behavior of the hysteresis loops performed with the field applied in the film plane. In particular, with increasing the Fe layer thickness the increase of remanence and the occurrence of a sudden variation of magnetization at zero field is predicted and observed [see Figs. 14(a)–14(d)].

On the basis of the previous results we can conclude that the model gives a good qualitative prediction of the behavior of the magnetization processes in Fe/FePt exchange-coupled bilayers with perpendicular anisotropy with the field applied both parallel and perpendicular to the film plane. We have shown that the predictions of the model become quantitatively significant by reasonably modifying key parameters, that is, the effective values of the saturation magnetization and demagnetizing factor of the soft layer, which cannot be directly measured.

V. FERH/FEPT BILAYER: MAGNETIC PHASE DIAGRAM AND HYSTERESIS LOOPS

In order to have a further check of the consistency of our model we apply it to the FeRh/FePt bilayer system and compare the results with those obtained by Guslienko *et al.* (Ref. 14). The materials parameters are deduced initially on the basis of the information given in the theoretical section of Ref. 14, that is for the soft FeRh layer $M_1=1.27$ MA/m, $K_1=0$ J/m^3, $A_1=1.6\times10^{-11}$ J/m; and for the hard FePt layer $M_2=1.1$ MA/m, $K_2=2$ MJ/m^3, $A_2=8\times10^{-12}$ J/m. However, different values of the exchange constants, that is, $A_1=A_2=1.25\times10^{-11}$ J/m ($J_{s1}=J_{s2}=10^{-20}$ J, $a=c=0.4\times10^{-9}$ m) are utilized in the section of Ref. 14, where the results of numerical calculations are reported. Therefore we calculate the phase diagram of FeRh/FePt bilayer in the two cases (Fig. 16), by assuming an intermediate interface coupling with respect to the bulk exchange coupling constants of the two phases (in the second case, it coincides with the values of the two bulk exchange constants A_1 and A_2) and on the basis of expression (18) for the critical susceptibility. It should be remarked that in our model index 1 refers to the soft and index 2 to the hard phase, while Guslienko *et al.*[14] adopted the opposite rule (see Fig. 6.)

To calculate the hysteresis loops corresponding to numerical calculations of Ref. 14 we need to solve the Euler Eqs. (13). However, due to the large values of the considered thicknesses for the FeRh/FePt bilayer ($t_1=80$ nm and t_2

=40 nm), we cannot utilize the shooting method to find the solutions: The precision required in determining the starting angle ϑ_1 is indeed too large for the available computation instruments. Then we adopt a one-dimensional finite element method (FEM) with linear shape functions, for directly minimizing the energy integral (12). Figure 3(a) shows the hysteresis loop calculated assuming an interface coupling J_s with the same value of bulk coupling $J_{s\text{-bulk}}$. The behavior of the $\vartheta(x)$ function in correspondence to different magnetic field values along the hysteresis loop is shown in Fig. 3(b).

From the plot of hysteresis loop reported in Fig. 3(a) one can observe that, after the occurrence of reversal at H_{c2}, the magnetization state is not completely saturated in the direction opposite to that of saturation (negative x axis). This fact can be recognized by examining the two $\vartheta(x)$ curves of Fig. 3(b) that correspond to $H=H_{c2}$. The nucleation field turns out $H=-H^*_{c1}=1.26$ MA/m. A peculiar characteristic of the hysteresis loop of Fig. 3(a) is the linearity of the different sections, which is related to the fact that the deviations from constant values in the configuration of magnetic moments [Fig. 3(b)] are concentrated in a thin interfacial region. The thickness of this region is comparable to an exchange length parameter depending on both exchange and effective anisotropy energy densities. This system resembles the case of a Bloch wall at the hard/soft interface.

The effect of a reduced interface coupling on the switching characteristic of the bilayer is analyzed in Fig. 5, which shows the reversal field H_{c2} as a function of the interface exchange coupling constant J_s. This figure can be directly compared with the analogous reported in Ref. 14. One may notice here the extreme sensitivity of the reversal field H_{c2} to the interface exchange coupling, at least for weak coupling: In the limit $J_s \rightarrow 0$ one has $H_{c2} \rightarrow H_{A2}=2L_2/(\mu_0 M_2)$, while, in the opposite limit $J_s \rightarrow J_{s\text{-strong}}=\infty$, H_{c2} tends to an asymptotic value which is characteristic of the (strongly coupled) composite system. In the intermediate coupling region, the influence that the presence of an (even weakly) exchange-coupled soft material exerts on the phenomenon of nucleation and reversal in the whole composite system becomes very evident. This situation can be analyzed even considering the angle difference $(\vartheta_{0^+}-\vartheta_{0^-})$ at the hard/soft interface, which increases on diminishing J_s, while it tends to vanish in the "strong" coupling limit.

In the case of the FeRh/FePt bilayer and for enough small values of constant ν, Eq. (17) admits two solutions lying between the extrema

$$H_{\min} = - H^*_{\max} = - \frac{2L_2}{\mu_0 M_2} = - 1.79 \text{ MA/m}$$

$$H_{\max} = - H^*_{\min} = \frac{2L_1}{\mu_0 M_1} = - 1.27 \text{ MA/m}.$$

One obtains the coincidence of the two solutions for a given critical value ν_c, corresponding to the critical value J_{sc} of the exchange coupling constant, which, in this case, is $J_{\text{sc}}/J_{s\text{-bulk}}=0.0249$ in normalized units. The two coincident critical fields $H_{c12}=H_{c2}=-1.525$ MA/m correspond to this critical value. Figure 7(a) shows the major hysteresis loop for the FeRh/FePt bilayer in the case $J_s/J_{s\text{-bulk}}=0.02 < J_{\text{sc}}/J_{s\text{-bulk}}$, with the two distinct critical fields $H_{c12}= -1.355$ MA/m and $H_{c2}=-1.7$ MA/m. The inset of Fig. 7(a) shows an enlarged-scale portion of the hysteresis loop in the region close to the critical field H_{c12}, where a non-linearity of the magnetization curve is evidenced. Figure 7(b) reports the behavior of the $\vartheta(x)$ and the $\psi(x)=\pi-\vartheta(x)$ functions, corresponding to the magnetic field value $H=-H^*= -1.34$ MA/m, which is slightly below (in absolute value) the critical field H_{c12}. One may notice the small bending of the functions near the hard/soft interface, which disappears in the case of ideally decoupled system.

VI. CONCLUSIONS

A continuum micromagnetic model has been developed to predict the magnetic behavior of exchange-coupled bilayers and multilayers having the magnetization perpendicular to the film plane. The model, formulated for a "strong" exchange interface coupling, has also been extended to the case of a reduced coupling.

Similar to the case of the planar anisotropy, it has been shown that the one-dimensional approach is appropriate for the description of the magnetization reversal process. As a consequence, the same mathematical expressions obtained in the case of in-plane easy axis are valid, provided that the anisotropy constant of each phase is replaced by an effective quantity, which includes the shape anisotropy.

The magnetic phase diagram, drawn in terms of soft- and hard-layer thickness, consists of two magnetic regions corresponding to the rigid (RM) and to the exchange-spring (ES) magnet.

A two-stage magnetization reversal, characterized by the nucleation field H_{c1} and the reversal field H_{c2}, has been found, as generally observed for hard/soft exchange spring systems. An implicit expression has been derived for the nucleation field H_{c1} that, differently form the planar case, can assume either positive or negative values.

The hysteresis loops corresponding to the different magnetic regions, have also been determined and traced as continuous curves, including both the stable and the unstable equilibrium states.

The perpendicular geometry, which implies a strong anisotropy also for the soft phase due to the shape contribution, has important consequences. In particular, the variation of magnetization orientation is confined within narrow regions, of the order of the exchange lengths, around the interface. Moreover, the system displays the following peculiar features: (i) The dependence of the critical fields on the layer thickness is strong within the range of exchange lengths; (ii) The critical fields tend to saturate with increasing layer thicknesses; and (iii) The hysteresis loops, in the case of layer thicknesses much larger than the respective exchange lengths, show linear demagnetizing curves as two decoupled phases (although the interface coupling strongly affects the values of the reversal field).

It is also found that, with increasing soft layer thickness, the reversal field H_{c2} is strongly reduced with respect to the hard layer effective anisotropy field. The reduction tends to an asymptotic value and it is of the order of 70%, even with a very thin soft layer. Moreover, the analytical expression of the reversal field is obtained in the limiting case of large soft and hard layer thickness.

Model predictions have been compared to the data obtained from a series of Fe/FePt bilayers prepared by sputtering. The model gives a good qualitative description of the behavior of magnetization and demagnetization processes with the field applied both parallel and perpendicular to the film plane. The quantitative agreement is improved by varying two key parameters, which are the values of the saturation magnetization and demagnetizing factor of the soft layer.

The application of the model to FeRh/FePt bilayers, taking into account a reduced interlayer coupling, gives a good description of its magnetic behavior, in agreement with the results obtained by Guslienko *et al.* (Ref. 14). This is a further confirmation of the widespread reliability of our model to describe the magnetization processes in various exchange-coupled systems.

ACKNOWLEDGMENTS

The present work has been supported by a FIRB Project of the Italian Ministry of Education and Research, entitled "Microsystems based on magnetic materials structured on a nanoscopic scale" and by a PRIN Project entitled "Magnetic nanostructures for patterned quantized magnetic devices."

APPENDIX

We consider an infinitely extended bilayer with perpendicular anisotropy and we assume that the magnetization is uniform on each plane of the system. In this case the Gibbs free energy density for a film portion with unitary area is

$$G = \sum_{i=1,2} (-1)^i \int_{x_0}^{x_i} F_i dx,$$

where $(i=1,2)$

$$F_i = A_i\left[\left(\frac{\partial\vartheta}{\partial x}\right)^2 + \sin^2\vartheta\left(\frac{\partial\varphi}{\partial x}\right)^2\right] + \mu_0 M_i H^* \cos\vartheta + L_i \sin^2\vartheta.$$

The function $\varphi(x)$ represents the angle between the projection of magnetization in the y-z plane and the z axis (azimuthal angle). If we suppose a "strong" exchange coupling at the hard/soft interface, this hypothesis leads to the conditions of continuity for the $\varphi(x)$ and the $\vartheta(x)$ functions

$$\varphi(x_{0^-}) = \varphi(x_{0^+}) \quad \vartheta(x_{0^-}) = \vartheta(x_{0^+}),$$

with the exception of the particular case $\vartheta(x_0)=0,\pi$.

The equilibrium configurations of the magnetization correspond to configurations of minimum energy and thus they cause the functional of free energy to be stationary. That is, $\delta G=0$, where the variation of the functional is calculated at the variations $\delta\varphi(x)$ and $\delta\vartheta(x)$, complying with the conditions of continuity

$$\delta\varphi(x_{0^-}) = \delta\varphi(x_{0^+}) \quad \delta\vartheta(x_{0^-}) = \delta\vartheta(x_{0^+}).$$

By calculating the variation of the functional and integrating by parts one obtains

$$\delta G = \sum_{i=1,2} (-1)^i \left\{ \left[\frac{\partial F_i}{\partial \dot\vartheta}\right]_{x_i} \delta\vartheta_i + \left[\frac{\partial F_i}{\partial \dot\varphi}\right]_{x_i} \delta\varphi_i - \left[\frac{\partial F_i}{\partial \dot\vartheta}\right]_{x_0} \delta\vartheta_0 - \left[\frac{\partial F_i}{\partial \dot\varphi}\right]_{x_0} \delta\varphi_0 + \int_{x_0}^{x_i} \left[\left(\frac{\partial F_i}{\partial \vartheta} - \frac{d}{dx}\frac{\partial F_i}{\partial \dot\vartheta}\right)\delta\vartheta - \left(\frac{d}{dx}\frac{\partial F_i}{\partial \dot\varphi}\right)\delta\varphi\right] dx \right\}.$$

By choosing $\vartheta(x)$ and $\varphi(x)$ functions for which only their variation inside the considered regions is nonvanishing, one obtains that the stationary solutions must satisfy the Euler equations

$$\frac{\partial F}{\partial\vartheta} - \frac{d}{dx}\frac{\partial F}{\partial\dot\vartheta} = 0 \quad \frac{d}{dx}\frac{\partial F_i}{\partial\dot\varphi} = 0.$$

From the second equation we deduce in particular

$$\sin^2\vartheta \frac{d\varphi}{dx} = \text{const.} \tag{A1}$$

If we consider now only functions $\vartheta(x)$ and $\varphi(x)$ satisfying the Euler equations, and impose that exclusively the extremal variation $\delta\varphi_i$ is nonvanishing, we obtain

$$\left[\frac{\partial F_i}{\partial\dot\varphi}\right]_{x_i} = 0,$$

from which

$$\sin^2\vartheta_1 \left.\frac{d\varphi}{dx}\right|_{x_1} = 0, \quad \sin^2\vartheta_2 \left.\frac{d\varphi}{dx}\right|_{x_2} = 0. \tag{A2}$$

The occurrence of conditions (A1) and (A2) requires that (by assuming $\vartheta \neq 0$ in general)

$$\frac{d\varphi}{dx} = 0,$$

and hence: $\varphi(x)=\text{const}$. In the case $\vartheta=0$, the φ angle has no particular meaning and may be assumed to be zero. By choosing an opportune z-axis orientation one may set the particular value $\varphi(x)=0$, while the $\vartheta(x)$ function satisfies the same conditions achieved in the case of the planar system, that is, the Euler Eqs. (3) with the boundary conditions (4).

[1] E. F. Kneller and R. Hawig, IEEE Trans. Magn. **27**, 3588 (1991).

[2] M. Solzi, M. Ghidini, and G. Asti, in *Magnetic Nanostructures*, edited by H. S. Nalwa (Amer. Scient. Publ., Stevenson Ranch, CA, 2002), Chap. 4, p. 124.

[3] R. Skomski, J. Appl. Phys. **76**, 7059 (1994).

[4] J. U. Thiele, S. Maat, and E. E. Fullerton, Appl. Phys. Lett. **82**, 2859 (2003).

[5] J.-U. Thiele, S. Maat, J. L. Robertson, and E. E. Fullerton, IEEE Trans. Magn. **40**, 2537 (2004).

[6] A. Moser, K. Takano, D. T. Margulies, M. Albrecht, Y. Sonobe, Y. Ikeda, S. Sun, and E. E. Fullerton, J. Phys. D **35**, R157 (2002).

[7] R. H. Victora and Xiao Shen, IEEE Trans. Magn. **41**, 537 (2005).

[8] D. Suess, T. Schrefl, R. Dittrich, M. Kirschner, F. Dorfbauer, G. Hrkac, and J. Fidler, J. Magn. Magn. Mater. **290–291**, 551 (2005).

[9] D. Niarchos, Sens. Actuators, A **109**, 166 (2003).

[10] M. R. J. Gibbs, J. Magn. Magn. Mater. **290–291**, 1298 (2005).

[11] O. Cugat, J. Delamare, and G. Reyne, IEEE Trans. Magn. **39**, 3607 (2003).

[12] C. T. Pan and S. C. Shen, J. Magn. Magn. Mater. **285**, 422 (2005).

[13] G. Asti, M. Solzi, M. Ghidini, and F. M. Neri, Phys. Rev. B **69**, 174401 (2004).

[14] K. Yu. Guslienko, O. Chubykalo-Fesenko, O. Mryasov, R. Chantrell, and D. Weller, Phys. Rev. B **70**, 104405 (2004).

[15] F. Garcia-Sanchez, O. Chubykalo-Fesenko, O. N. Myrasov, R. W. Chantrell, and K. Yu. Guslienko, J. Appl. Phys. **97**, 10J101 (2005).

[16] X. Hu, T. Yorozu, S. Honma, and Y. Kawazoe, IEEE Trans. Magn. **29**, 3790 (1993).

[17] A. Aharoni, *Introduction to the Theory of Ferromagnetism* (Clarendon Press, Oxford, 1996).

[18] F. B. Hagedorn, J. Appl. Phys. **41**, 2491 (1970).

[19] C. Abraham, Phys. Rev. **135**, A1269 (1964).

[20] G. Asti, C. Pernechele, R. Pellicelli, and M. Solzi (unpublished).

[21] F. Casoli, F. Albertini, L. Pareti, S. Fabbrici, L. Nasi, C. Bocchi, and R. Ciprian, IEEE Trans. Magn. **41** (10), 3223 (2005).

[22] F. Casoli, F. Albertini, S. Fabbrici, C. Bocchi, L. Nasi, R. Ciprian, and L. Pareti, IEEE Trans. Magn. **41** (10), 3877 (2005).

[23] O. A. Ivanov, L. V. Solina, V. A. Demshina, and L. M. Magat, Fiz. Met. Metalloved. **35**, 81 (1973).

[24] J. S. Chen, Y. Xu, and J. P. Wang, J. Appl. Phys. **93**, 1661 (2003).

[25] T. Suzuki, K. Harada, N. Honda, and K. Ouchi, J. Magn. Magn. Mater. **193**, 85 (1999).

[26] T. Shima, K. Takanashi, Y. K. Takahashi, and K. Hono, Appl. Phys. Lett. **81**, 1050 (2002).

[27] M. Watanabe and M. Homma, Jpn. J. Appl. Phys., Part 2 **35**, L1264 (1996).

[28] M. L. Yan, N. Powers, and D. J. Sellmyer, J. Appl. Phys. **93**, 8292 (2003).

[29] S. Okamoto, N. Kikuchi, O. Kitakami, T. Miyazaki, Y. Shimada, and K. Fukamichi, Phys. Rev. B **66**, 024413 (2002).

[30] H. Kanazawa, G. Lauhoff, and T. Suzuki, J. Appl. Phys. **87**, 6143 (2000).

[31] Yu. V. Goryunov, N. N. Garif'yanov, G. G. Khaliullin, I. A. Garifullin, L. R. Tagirov, F. Schreiber, T. Muhge, and H. Zabel, Phys. Rev. B **52**, 13450 (1995).

[32] F. Albertini, L. Nasi, F. Casoli, and L. Pareti (unpublished).

[33] J. S. Jiang, J. E. Pearson, Z. Y. Liu, B. Kabius, S. Trasobares, D. J. Miller, S. D. Bader, D. R. Lee, D. Haskel, G. Srajer, and J. P. Liu, J. Appl. Phys. **97**, 10K311 (2005).